Wall-collision effect on optically polarized atoms in small and hot vapor cells

Yue Chang* and Jie Qin
Beijing Automation Control Equipment Institute, Beijing 100074, China
and Quantum Technology R&D Center of China Aerospace Science and Industry Corporation, Beijing 100074, China

(Received 26 May 2023; revised 22 December 2023; accepted 24 January 2024; published 16 February 2024)

In atomic vapor cells, atoms collide with the inner surface, causing their spin to randomize on the walls. This wall-depolarizing effect can be diffusive and it becomes more pronounced in smaller vapor cells under high temperatures. In this work we investigate the polarization of optically pumped alkali-metal atoms in a millimeter-sized cell heated to 150 °C. We consider two extreme boundary conditions, fully depolarizing and nondepolarizing boundaries, and we provide an analytical estimation of the polarization difference between them. In the nondepolarizing case, the pump beam's absorption is proportional to the average atomic polarization. However, for fully depolarizing walls, the absorption peak may correspond to a polarization minimum. To mitigate the wall effect, we propose reducing the pump beam's diameter while maintaining the pump power to prevent illumination of the cell wall and increase the pump intensity in the central area. This is crucial for compact vapor-cell devices where the laser frequency cannot be detuned since it is locked to the absorption peaks. Additionally, we analyze the wall-depolarizing effect on the performance of an alkali-metal atomic magnetometer operating in the spin-exchange relaxation-free regime. We show that the signal strength is highly limited by wall collisions and we provide an upper bound for it.

DOI: 10.1103/PhysRevA.109.023113

I. INTRODUCTION

Optically polarized atoms play a crucial role in various fields, including magnetometry [1–3], noble-gas hyperpolarization [4–7], atomic clocks [8,9], quantum optics, and quantum information [10–12], as well as fundamental physics [13–15]. Typically, alkali-metal atoms are confined in a vapor cell and illuminated by a laser beam to transfer the light's polarization to the atoms' spins [16,17]. However, the atomic polarization can be limited by collisions with the inner cell walls. In particular, the spin of alkali-metal atoms can become almost fully randomized when colliding with the bare glass wall of the cell [18], and through atom-atom collisions this depolarization effect can spread to other parts of the vapor cell with relatively high atomic density or enough buffer gas. This boundary effect on the overall polarization is more significant in small and hot cells (we focus here on vapor cells whose size is much larger than the laser's wavelength, while the nanometric cells can also be used to study fundamental physics [19,20] and for sensing applications [21,22]). To mitigate this depolarization effect, antirelaxation coatings with a chemically inert substance such as paraffin can be used. However, paraffin is not stable above 80 °C and thus it is not widely used in commercial applications where the small vapor cell is usually heated to a relatively high temperature. The development of coatings that can work effectively and remain stable at high temperatures is still a challenge [18,23,24].

In uncoated vapor cells, ways to mitigate the wall-depolarizing effect include the use of a buffer gas, such as nitrogen gas, to slow down the motion of atoms by increasing the time spent colliding with the buffer gas, and thus the rate at which they reach the cell wall is reduced [16]. Detuning the pump laser can also reduce the wall effect by decreasing the optical depth and thus the light absorbed by the walls [25]. Most studies on how wall collision affects polarization focus on large (centimeter scale) or low-temperature cells, where the wall effect is treated as a constant contribution Γ_{wall} to the longitudinal decay rate Γ_1, accounting for the slowest diffusion mode [23,26]. In this paper we systematically study the wall-collision effect on small (millimeter scale) and hot (150 °C) alkali-metal vapor cells. By numerically solving the diffusion equation [6,27] with the depolarizing boundary condition, we find that the wall effect may be underestimated when considering only the slowest diffusion mode. We compare the average polarization P_{av} in depolarizing-wall cells with that in nondepolarizing-wall cells, obtaining an analytical ratio between these two polarizations as a function of the diffusion constant D, the longitudinal decay rate Γ_1, the optical pumping rate R_{op}, and the system size L. The polarization for depolarizing walls can be much smaller than that with nondepolarizing walls even if Γ_{wall} is added to Γ_1 in the nondepolarizing-wall case.

The laser beam's propagation is also considered. We prove that the polarization P_{av} in nondepolarizing-wall cells illuminated by uniformly distributed laser beams is independent of the diffusion constant and it is proportional to the pump laser's absorption. Thus, P_{av} can be acquired from the absorption spectrum. However, this relation does not hold for depolarizing boundaries, where an absorption peak may correspond to a local minimum of polarization due to light absorption by the depolarizing wall. We define a quantity η_{loss} to characterize

*yuechang7@gmail.com

the pump beam's loss on the cell walls, which decreases when the pump laser is detuned from the corresponding transition [25]. Reducing the diameter of the laser beam with the same input power also weakens the wall-depolarizing effect on the overall cell, resulting in more polarization achieved with a relatively small input power. This is advantageous to compact vapor-cell-based devices where the pump laser's frequency is locked to the absorption peaks.

Finally, we study the wall-depolarization effect on spin-exchange relaxation-free (SERF) magnetometers [28–30], which are one of the most sensitive magnetic-field sensors that typically operate at high temperatures. When integrating an array of these sensors, the spatial distribution of the magnetic field can be detected, requiring a small volume to enhance spatial resolution. By exposing the SERF magnetometer to a small transverse magnetic field, the linear response P_x is extracted. If the atoms are homogeneously polarized, the transverse signal P_x is maximum when the longitudinal polarization $P_{\rm av}$ is $1/2$ [23]. However, including diffusion, the largest P_x occurs at a smaller $P_{\rm av} < 1/2$ for depolarizing boundaries. Moreover, when the wall is perfectly coated to prevent depolarization, the signal P_x can increase by an order of magnitude, even with the depolarizing-wall cell filled with thousands of Torr of nitrogen gas. We provide an upper bound of the optimal P_x for the depolarizing-wall case, which facilitates efficient signal magnitude estimation without having to solve diffusion equations for atomic spins and Maxwell equations for light propagation. We also find that reducing the illuminated area can enhance the transverse signal P_x.

The organization of this paper is as follows. In Sec. II we begin by examining the case where the vapor cell is uniformly illuminated. Using ^{87}Rb as an example (the case for ^{133}Cs is also shown briefly in Appendix C), we solve the atomic diffusion equation and the light-propagation equation under two extreme boundary conditions: fully depolarizing and nondepolarizing walls. We present the distribution of the polarization and the light intensity in a cylindrical cell, as well as an analysis of the average polarization and the light transmission. Additionally, we define the portion $\eta_{\rm loss}$ of light absorbed by the cell walls. In Sec. III we investigate the transverse signal P_x of a SERF magnetometer under various physical conditions and analyze the optimal P_x. Moving on to a partially illuminated vapor cell, Sec. IV examines the dependence of the polarization $P_{\rm av}$, the light transmission, and the performance of SERF magnetometers on the diameter of the laser beam. In Sec. V we summarize our work.

II. ATOMIC POLARIZATION AND LIGHT TRANSMISSION

In this section we will solve the light-propagation equation along with the atomic diffusion equation and obtain the light transmission and the atom's polarization. Without loss of generality, we assume that the vapor cell is cylindrical with a length of L and a radius of R, as shown in Fig. 1. The pump beam propagates in the z direction and has a cross-section radius of r_L. The longitudinal axis of the cylindrical cell is the same as the laser beam's, so the system has cylindrical symmetry. Therefore, the polarization and light intensity I within the cell are functions of the longitudinal coordinate $z \in [0, L]$ and radial distance $r \in [0, R]$. In the high-temperature

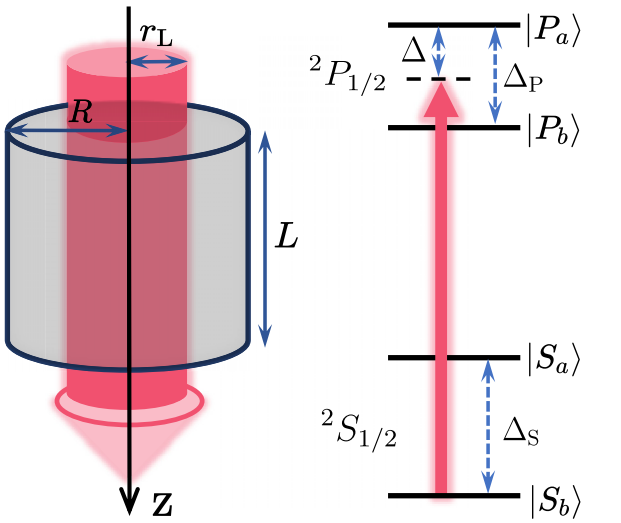

FIG. 1. Schematic of a cylindrical vapor cell (gray cylinder) optically pumped by a laser beam (red beam) with a radius of r_L. The cell has a longitudinal length of L and a radius of R and is filled with alkali-metal atoms and buffer gas. The energy level of the alkali-metal atom is shown on the right. The pump laser couples to the ground states $^2S_{1/2}$ and the first excited states $^2P_{1/2}$ ($D1$ transition) with a detuning of Δ. Due to the hyperfine interaction, the ground (excited) states are split into two manifolds $|S_a\rangle$ and $|S_b\rangle$ ($|P_a\rangle$ and $|P_b\rangle$), respectively, with an energy difference of Δ_S (Δ_P).

limit, the atomic state can be well approximated by the spin-temperature distribution [6,28] and we can characterize the atomic polarization $\langle F_z\rangle$ by the electronic polarization $P_e \equiv 2\langle S_z\rangle$ and the slow-down factor $q(P_e) \equiv \langle F_z\rangle/\langle S_z\rangle$ is a function of P_e. Here F_z (S_z) is the total (electronic) spin in the z direction. After eliminating adiabatically the excited states [31] in the alkali-metal atom's master equation [6] and taking the average value of F_z (note that $\langle F_z\rangle = q(P_e)\langle S_z\rangle$), $P_e(z, r)$ in the steady state satisfies the equation

$$D\nabla^2 q(P_e)P_e - (R_{\rm op} + \Gamma_{\rm rel})P_e + R_{\rm op} = 0, \tag{1}$$

where D is the diffusion constant, $\Gamma_{\rm rel}$ is the atom-collision-induced spin-destruction rate, and $R_{\rm op} = g_P\mathcal{L}(\Delta)I$ is the optical pumping rate. Here g_P is the square of the dipole moment $\langle d\rangle$ and $\mathcal{L}(\Delta)$ the line shape, which will be explicitly given later. Note that we assume the collisions are strong enough so that the atoms are in a local spin-temperature distribution with the spin temperature varying as a function of the atom's coordinate (z, r). Additionally, we consider a cell filled with nitrogen as the buffer gas to weaken the wall effect and suppress radiation trapping [32]. This ensures that the atom is confined so that its motion is diffusive instead of ballistic. Moreover, alkali-metal atoms excited by the laser beam decay to the ground states mostly via colliding with the N_2 molecules. Thus, nearly no photons are emitted during this process, making it safe to neglected the reflection of the laser beam. Consequently, we can linearize the forward-propagation equation of light as follows [23,31]:

$$\partial_z I = -g_I\mathcal{L}(\Delta)I(1 - P_e). \tag{2}$$

Here $g_I = n_A k\langle d\rangle^2$, where n_A is the density of alkali-metal atoms and k is the laser's wavelength.

For ^{87}Rb, the slow-down factor [23,31]

$$q(P_e) = \frac{6 + 2P_e^2}{1 + P_e^2} \tag{3}$$

and the line shape can be described as a sum of four Lorentzian functions corresponding to four transitions between two ground-state and two excited-state manifolds. This is given by [23,31]

$$\mathcal{L}(\Delta) = \frac{\Gamma_L}{16\pi}\left(\frac{5}{\Delta^2 + \Gamma_L^2} + \frac{5}{(\Delta - \Delta_S - \Delta_P)^2 + \Gamma_L^2} + \frac{5}{(\Delta - \Delta_S)^2 + \Gamma_L^2} + \frac{1}{(\Delta - \Delta_P)^2 + \Gamma_L^2}\right), \tag{4}$$

where Γ_L is the decay rate of the excited states and is proportional to the density of nitrogen gas. We consider the conditions 150 °C, 200 Torr N_2, $L = 2R = 2$ mm, and $\Delta = 0$ and plot the polarization $P_e(z, r)$ and normalized light intensity $I(z, r)/I_0$ in Fig. 2. Here $I_0 \equiv I(0, 0)$ represents the laser intensity at the incident plane, and the input laser power is 0.5 mW, illuminating uniformly on the entire cell ($r_L = R$). For depolarizing walls, the polarization $P_e^{\rm de}(z, r)$ [Fig. 2(a)] is maximum at the center $r = 0$ and decays towards the boundaries due to depolarization of the walls and decrease in light density. The decrease in light intensity is shown in Fig. 2(b), where the intensity $I^{\rm de}(z, r)$ monotonically decreases along the propagation direction and decays from the center to the boundaries. To illustrate this explicitly, Figs. 2(c) and 2(d) show the decay of $I^{\rm de}(z, r)$ in the radical and longitudinal directions, respectively. For comparison, we show $P_e^{\rm nonde}(z, r)$ and $I^{\rm nonde}(z, r)/I_0$ for nondepolarizing walls in Figs. 2(e) and 2(f), respectively. Here $P_e^{\rm nonde}(z, r)$ and $I^{\rm nonde}(z, r)$ change only in the pump laser's propagation direction, and the atomic spins are nearly fully polarized (approximately 0.99), leading to a close-to-unity $I^{\rm nonde}(z, r)/I_0$.

By integrating Eqs. (1) and (2) we obtain

$$1 - T = \frac{g_I}{I_{\rm in} g_P}\left(V\Gamma_{\rm rel}P_{\rm av} - D\oint d\mathbf{S}\cdot\nabla[q(P_e)P_e]\right), \tag{5}$$

where

$$T = \frac{\int_{z=L} dS\, I(r, L)}{I_{\rm in}} \tag{6}$$

represents the transmission probability, S is the cell wall,

$$I_{\rm in} = \int_{z=0} dS\, I(r, 0) \tag{7}$$

is the total input power, and $P_{\rm av}$ is the average polarization over the cell volume V,

$$P_{\rm av} = \frac{1}{V}\int_V dV\, P_e. \tag{8}$$

If the wall does not depolarize spins ($\nabla P_e|_S = 0$), we obtain a simplified expression

$$1 - T = \frac{V\Gamma_{\rm rel} g_I}{I_{\rm in} g_P} P_{\rm av} \tag{9}$$

since $\nabla[q(P_e)P_e] = \partial_{P_e}[q(P_e)P_e]\nabla P_e$. This implies that the absorbed light is entirely transferred to the spin polarization $P_{\rm av}$ and that they have a one-to-one correspondence. Additionally,

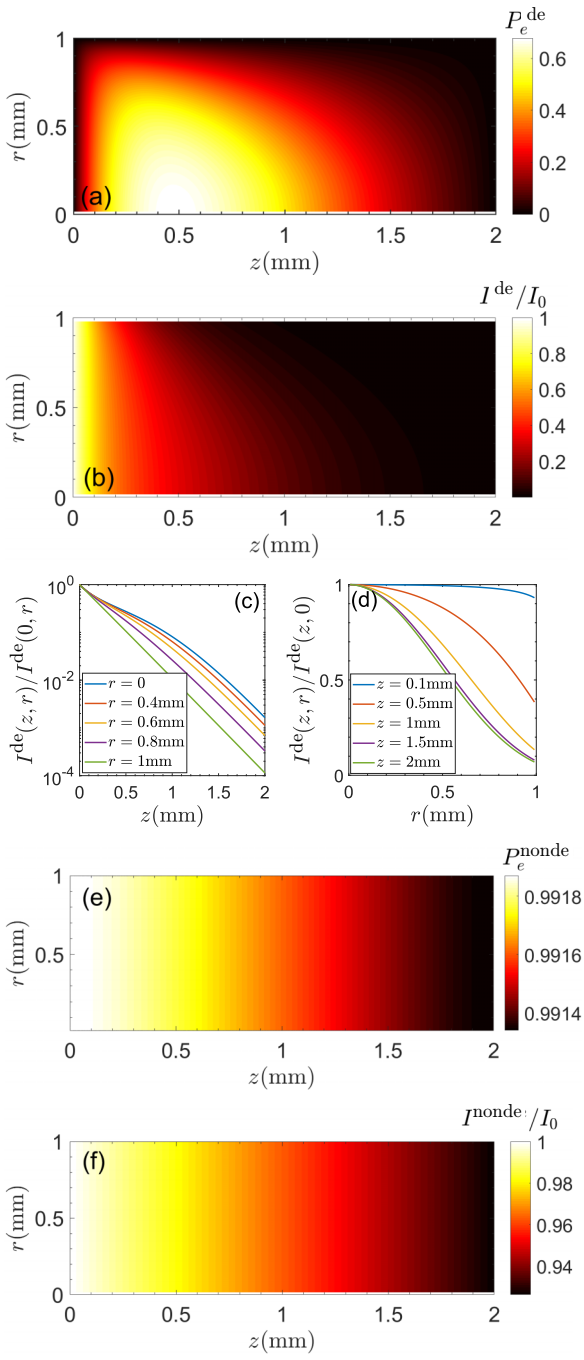

FIG. 2. Polarization $P_e(z, r)$ and light intensity $I(z, r)$ distributions within the ^{87}Rb vapor cell for (a)–(d) depolarizing and (e) and (f) nondepolarizing boundaries. Plots of (c) r and (d) z increase from the top curve to the bottom.

it can be proved (see Appendix A) that the absorption or polarization peak occurs at $\partial_\Delta \mathcal{L}(\Delta) = 0$.

In the case of depolarizing walls, $P_e|_S = 0$ and the relation (9) no longer holds. At the cell walls, $\nabla[q(P_e)P_e]$ is negative in the direction of $d\mathbf{S}$ ($\partial_{P_e}[q(P_e)P_e] = 2\partial_{P_e}\langle F_z\rangle > 0$) and $\oint d\mathbf{S}\cdot\nabla[q(P_e)P_e] < 0$. Consequently, more light is absorbed for depolarizing boundaries, but some of it does not transfer to the spin polarization and is lost in the cell walls. To quantify

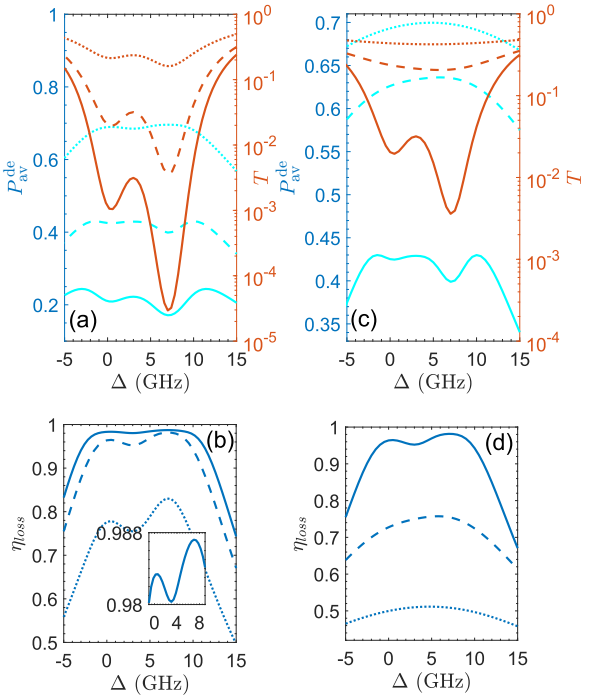

FIG. 3. Average polarization $P_{\rm av}$ of ^{87}Rb [light blue lines in (a) and (c)], transmission probability T [dark red lines in (a) and (c)], and the ratio $\eta_{\rm loss}$, representing the fraction of pump laser absorbed by the cell walls [in (b) and (d)] for depolarizing walls. In (a) and (b) the N_2 pressure is 200 Torr and the input powers are 0.5 mW (solid lines), 1 mW (dashed lines), and 3 mW (dotted lines). In contrast, in (c) and (d) the input power is fixed at 1 mW while the N_2 pressures are varied from 200 Torr (solid lines) to 500 Torr (dashed lines) and 1000 Torr (dotted lines). The inset in (b) explicitly shows the two absorption peaks of the light by the depolarizing walls. All other parameters are identical to those in Fig. 2.

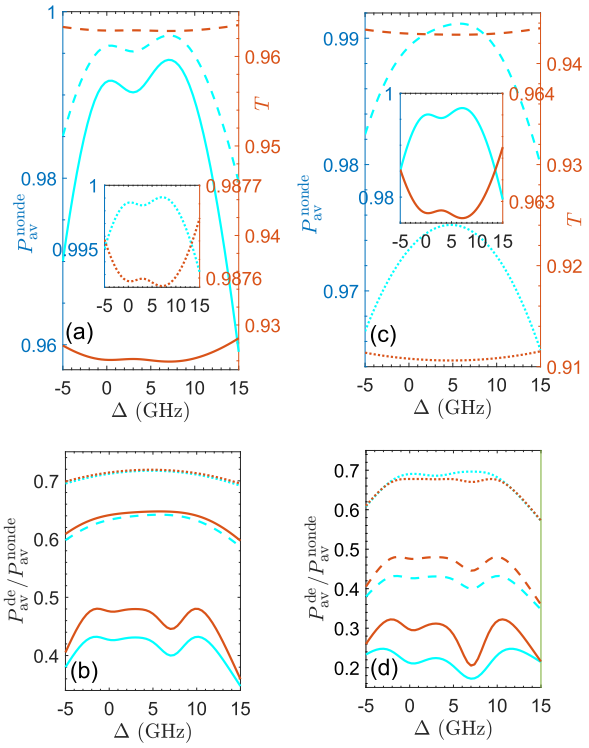

FIG. 4. Average polarization $P_{\rm av}^{\rm nonde}$ of ^{87}Rb [light blue lines in (a) and (c)] and transmission probability T [dark red lines in (a) and (c)] for nondepolarizing walls. The ratio $P_{\rm av}^{\rm de}/P_{\rm av}^{\rm nonde}$ is shown in (c) and (d). Similar to Fig. 3, the N_2 pressure is fixed at 200 Torr in (a) and (b), while input powers of 0.5 mW (solid lines), 1 mW (dashed lines), and 3 mW (dotted lines) are used. In (c) and (d) the input power is fixed at 1 mW and N_2 pressures of 200 Torr (solid lines), 500 Torr (dashed lines), and 1000 Torr (dotted lines) are used. The remaining parameters are identical to those in Fig. 2. The numerical results are shown with blue (light gray) lines in (b) and (d), while the analytical estimation using Eq. (11) is shown with red (dark gray) lines. In this case, the slow-down factor q in Eq. (11) is fixed at 5.

this loss, we define the portion of light lost $\eta_{\rm loss}$ as follows:

$$\eta_{\rm loss} = 1 - T - \frac{V\Gamma_{\rm rel} g_I}{I_{\rm in} g_P} P_{\rm av}. \tag{10}$$

Here $\eta_{\rm loss}$ is the loss due to the spin randomized at the cell walls, leading to a faster spin decoherence and lower population of the dark state near the walls. As an overall effect, the wall collision decreases the longitudinal relaxation time of spins in the vapor cell. The absorbed light's helicity is not totally transferred to the atomic polarization and furthermore more photons are absorbed because of the lower polarization of atomic spins, resulting in less transmission of light. As a contrast, for nondepolarizing walls, $\eta_{\rm loss} = 0$, indicating that all of the absorbed photons can be utilized to polarize the atoms and no photons are "wasted" on the walls.

For different N_2 pressures and input powers, we show the average polarization $P_{\rm av}^{\rm de}$, the transmission probability T, and the loss $\eta_{\rm loss}$ in Fig. 3. For low gas pressures (200 Torr) and input powers (less than 3 mW), the transmission T has two minima at $\Delta \approx 0$ and $\Delta \approx \Delta_S$, respectively (the energy splitting in the excited states cannot be distinguished because $\Gamma_L \sim \Delta_P$), while the polarization $P_{\rm av}^{\rm de}$ is minimal at these two absorption peaks [Fig. 3(a)]. This is due to the large loss of light on the walls, as shown in Fig. 3(b), where the absorption of light by the wall is maximal at the resonant points 0 and Δ_S since the bare absorption length $\lambda_L \equiv [g_I \mathcal{L}(\Delta)]^{-1}$ of the laser is shortest (assuming the polarization is zero). This is also true for higher input powers. When the laser power increases to 3 mW, the wall-depolarizing effect is reduced since $P_{\rm av}^{\rm de}$ is higher, so the absorption-polarization relation is closer to the nondepolarizing-wall case and the absorption peaks correspond to polarization peaks. Furthermore, decreasing the diffusion constant D by increasing the N_2 pressure can also reduce the wall-depolarizing effect. In Figs. 3(c) and 3(d), when the nitrogen gas pressure is increased from 200 Torr to 500 Torr and 1000 Torr, the two absorption peaks and the two peaks in the loss $\eta_{\rm loss}$ merge into one peak since $\Gamma_L \sim \Delta_S$, where the polarization is maximal. With higher N_2 pressures, $P_{\rm av}^{\rm de}$ and T become higher, because the wall-depolarizing effect is smaller [Fig. 3(d)] while the absorption length λ_L is larger.

For comparison, the polarization and transmission for nondepolarizing walls are illustrated in Fig. 4. As proved in Appendix A, there exist absorption and polarization peaks at $\partial_\Delta \mathcal{L}(\Delta) = 0$. For low gas pressure (200 Torr), the polarization $P_{\rm av}^{\rm nonde}$ exhibits two peaks at $\Delta \approx 0$ and $\Delta \approx \Delta_S$,

corresponding to two transmission minima [Fig. 4(a)]. With increasing N_2 pressure, the two peaks become indistinguishable and both the polarization $P_{\rm av}^{\rm nonde}$ and the transmission T decrease [Fig. 4(c)]. The decrease in transmission is due to the increase in $\Gamma_{\rm rel}$, which exceeds the effect of λ_L's increment on the polarization. In the absence of depolarization on the walls, the transmission T is close to unity and the polarization $P_{\rm av}^{\rm nonde}$ is much larger than $P_{\rm av}^{\rm de}$. Therefore, the ratio $P_{\rm av}^{\rm de}/P_{\rm av}^{\rm nonde}$ can also be used to characterize the wall-depolarization effect, as plotted in Figs. 4(b) and 4(d) with blue lines. Like the light lost $\eta_{\rm loss}$, the ratio $P_{\rm av}^{\rm de}/P_{\rm av}^{\rm nonde}$ can be increased by detuning the pump laser, increasing the pump power, or increasing N_2 density. Apart from solving the nonlinear equations (1) and (2), this ratio $P_{\rm av}^{\rm de}/P_{\rm av}^{\rm nonde}$ can also be estimated as (see Appendix B for the derivation)

$$\frac{P_{\rm av}^{\rm de}}{P_{\rm av}^{\rm nonde}} \approx \sqrt{1-\frac{\lambda_D}{\lambda_L}}\left(1-2\frac{\lambda_D}{L}\right)\left(1-\frac{\lambda_D}{R}\right)^2, \tag{11}$$

where

$$\lambda_D = \sqrt{\frac{qD}{\Gamma_{\rm rel}+R_{\rm op}^0}}. \tag{12}$$

Here λ_D is the wall-depolarization length with $R_{\rm op}^0 \equiv g_P\mathcal{L}(\Delta)I_0$ and λ_L is the absorption length that is inversely proportional to the alkali-metal-atom density, illustrating that $P_{\rm av}^{\rm de}$ can be much smaller than $P_{\rm av}^{\rm nonde}$ for small and hot vapor cells (millimeter-scale cells at about 150 °C, for instance). The validity of this estimation requires the ratio λ_D/λ_L between the wall-depolarization length λ_D and the absorption length λ_L to be smaller than 1. The smaller the λ_D/λ_L, the better the analytical estimation, as shown in Figs. 4(b) and 4(d) with red lines. The ratio λ_D/λ_L can be reduced by increasing the incident light density I_0 or the detuning Δ from the resonant points, or decreasing the diffusion constant D. When λ_D/λ_L is not sufficiently small the approximation (11) is not perfect [solid lines in Figs. 4(b) and 4(d)], but it still provides an upper bound for $P_{\rm av}^{\rm de}/P_{\rm av}^{\rm nonde}$, since we have assumed that the light density I does not change much within the wall-depolarization length and λ_D consequently depends solely on the initial value I_0. Note that the slow-down factor q is a function of the local polarization $P_e(z,r)$ but a median value can be used to simplify the calculation. For ^{87}Rb, q varies between 4 (fully polarized) and 6 (zero polarization), and we take $q=5$ in Eq. (11).

Literally, a commonly used approach to account for the depolarizing-wall effect is to introduce a spin-depolarization rate $\Gamma_{\rm wall}$, which is determined by the lowest diffusion mode, to the longitudinal relaxation rate. In this study we investigate this method by substituting $\tilde{\Gamma}_{\rm rel} = \Gamma_{\rm rel} + \Gamma_{\rm wall}$ for the nondepolarizing-wall case. For cylindrical cells,

$$\Gamma_{\rm wall} = qD\left[\left(\frac{\pi}{L}\right)^2 + \left(\frac{\mu_1}{R}\right)^2\right], \tag{13}$$

where μ_1 is the first zero of the Bessel function of the first kind [25,33]. By taking the maximum value of $q=6$ in Eq. (13), we depict $\tilde{P}_{\rm av}^{\rm nonde}$ in Fig. 5 with red lines, while $P_{\rm av}^{\rm de}$ is shown with blue lines for comparison. Our findings reveal that, even with the inclusion of $\Gamma_{\rm wall}$ in $\Gamma_{\rm rel}$, the polarization $\tilde{P}_{\rm av}^{\rm nonde}$ can be significantly larger than $P_{\rm av}^{\rm de}$. Thus, this simplistic approach may underestimate the wall-depolarizing effect.

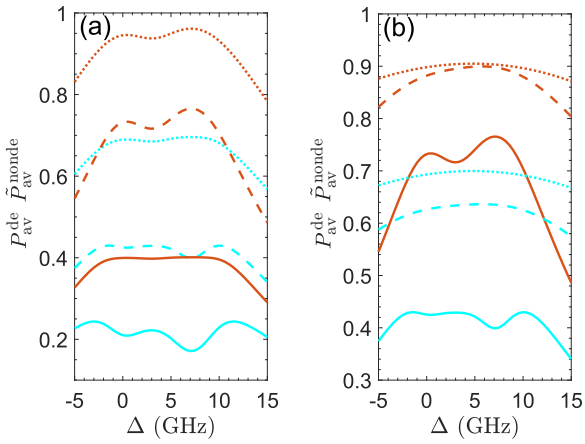

FIG. 5. Average polarization $\tilde{P}_{\rm av}^{\rm nonde}$ of ^{87}Rb (dark red lines) for nondepolarizing walls by including $\Gamma_{\rm wall}$ (with slow-down factor $q=6$) in the longitudinal decay. In comparison, $P_{\rm av}^{\rm de}$ is shown with light blue lines. Similar to Fig. 3, (a) displays the results for N_2 pressure of 200 Torr and input powers of 0.5 mW (solid lines), 1 mW (dashed lines), and 3 mW (dotted lines). In (b) the input power is constant at 1 mW, while the N_2 pressures vary among 200 Torr (solid lines), 500 Torr (dashed lines), and 1000 Torr (dotted lines). All other parameters remain unchanged from Fig. 2.

III. WALL EFFECT ON SERF MAGNETOMETERS

In this section we take SERF magnetometers [1,28,29] as an example to study the wall effect on the transverse signals $P_x \equiv 2\langle S_x\rangle$. Spin-exchange relaxation-free magnetometers are highly sensitive to magnetic fields and do not suffer from spin-exchange relaxation, which is a major source of spin decoherence in atomic magnetometers. In order to operate in the SERF regime, SERF magnetometers are typically used at high temperatures and low magnetic fields B. Here we assume that the magnetic field B is in the y direction and its induced energy splitting is much smaller than the spin-destruction rate $\Gamma_{\rm rel}$. As in Sec. II, we assume that the atomic system is approximately in a spin-temperature distribution. Taking the average value of F_x in the alkali-metal atom's master equation [6], to the first order of the small magnetic field B, P_x in the long-term limit satisfies the equation

$$D\nabla^2 q(P_x)P_x - (R_{\rm op}+\Gamma_{\rm rel})P_x + \gamma_e B P_e = 0, \tag{14}$$

where γ_e is the electron's gyromagnetic ratio and $\gamma_e B \ll \Gamma_{\rm rel}$. Note that here we have ignored the light shift induced by the pump laser, as it is usually compensated for by a magnetic field in the z direction in practical use.

The solution $P_x^{\rm de}(z,r)$ to Eq. (14) for depolarizing boundaries is depicted in Fig. 6(a), where the parameters used are the same as in Fig. 2(a). It can be observed in Fig. 6(a) that $P_x^{\rm de}(z,r)$ reaches its maximal value in the region where $P_e^{\rm de}(z,r) \approx 1/2$, which is consistent with the simple model of SERF magnetometers that disregards the light propagation and atomic diffusion. However, it should be noted that the

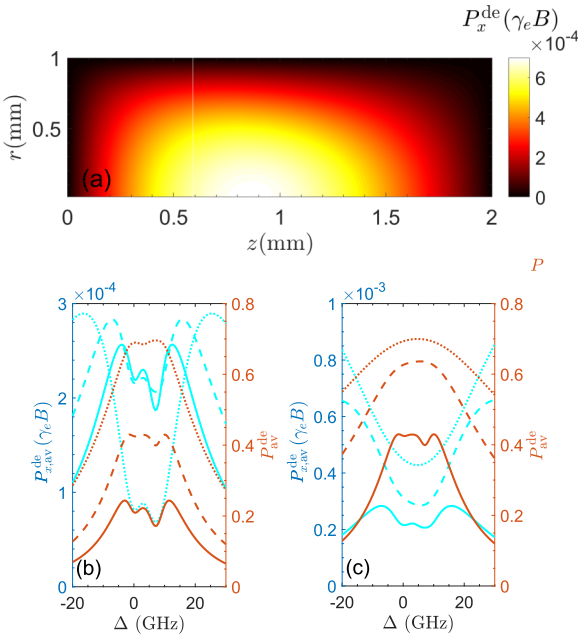

FIG. 6. (a) Spatial dependence of $P_x^{\rm de}(z,r)$ of ^{87}Rb for depolarizing walls, using the same parameters as in Fig. 2(a). (b) and (c) Average signal $P_{x,\rm av}^{\rm de}$ (light blue lines) and corresponding polarization $P_{\rm av}^{\rm de}$ (dark red lines). (b) Same as in Fig. 3, the N_2 pressure is 200 Torr and the input powers are 0.5 mW (solid lines), 1 mW (dashed lines), and 3 mW (dotted lines). (c) The input power is 1 mW and the N_2 pressures are 200 Torr (solid lines), 500 Torr (dashed lines), and 1000 Torr (dotted lines). All other parameters are the same as in Fig. 2.

maximum of the total transverse signal

$$P_{x,\rm av} \equiv \frac{1}{V}\int_V dV\, P_x \tag{15}$$

appears at $P_{\rm av}^{\rm de} < 1/2$ [see Figs. 6(b) and 6(c)]. This is because the polarization $P_e^{\rm de}(z,r)$ decays as it approaches the cell walls. For small $P_{\rm av}^{\rm de}$ [solid lines in Figs. 6(b) and 6(c)], the transverse signal $P_{x,\rm av}$ locally reaches its minimum at the absorption peaks, where $P_{\rm av}^{\rm de}$ is also locally minimal. This behavior is preserved even for the large input region, as depicted by the dashed and dotted lines in Figs. 6(b) and 6(c). This is in contrast to $P_{\rm av}^{\rm de}$, since with high input power, $P_{\rm av}^{\rm de}$ reaches a local maximum and exceeds 1/2 at the absorption peaks.

To increase the total transverse signal $P_{x,\rm av}$, one can enlarge the region where the electron polarization $P_e^{\rm de}(z,r)$ is approximately 1/2, since the transverse polarization $P_x^{\rm de}(z,r)$ is large in this region. This can be achieved by increasing the buffer gas density or by detuning the pump laser while increasing its power to compensate for the decrease in optical pumping rate. Optimal signals $\tilde{P}_{x,\rm av}^{\rm de}$ are obtained for different input powers of the pump laser by varying the detuning Δ for different N_2 pressures. As shown in Fig. 7(a), for a given N_2 pressure, the maximal signal $\tilde{P}_{x,\rm av}^{\rm de}$ saturates as the input power increases because the wall-depolarization length λ_D saturates and the region where $P_e^{\rm de}(z,r) \approx 1/2$ does not extend. With more N_2, the wall-depolarization length λ_D saturates at a smaller value and the region where $P_e^{\rm de}(z,r) \approx 1/2$ is further enlarged, resulting

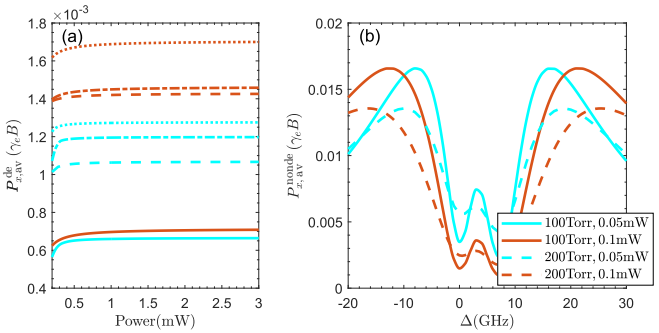

FIG. 7. (a) Transverse signal $\tilde{P}_{x,\rm av}^{\rm de}$ of ^{87}Rb as a function of the pump laser power at various N_2 pressures. The light blue lines represent the numerical results obtained by varying the detuning Δ, while the dark red lines represent the analytical estimation (16) that provides an upper bound for $\tilde{P}_{x,\rm av}^{\rm de}$ with a difference of no more than 30%. The N_2 pressures considered are 500 Torr (solid lines), 1000 Torr (dashed lines), 2000 Torr (dotted lines), and 3000 Torr (dash-dotted lines). The remaining parameters are the same as in Fig. 2(a). (b) Transverse signal $P_{x,\rm av}^{\rm nonde}$ for nondepolarizing walls at a temperature of 150 °C, where the light blue (dark red) lines are for an input of 0.05 mW (0.1 mW).

in a larger $\tilde{P}_{x,\rm av}^{\rm de}$ ($\tilde{P}_{x,\rm av}^{\rm de}|_{500\ \rm Torr} < \tilde{P}_{x,\rm av}^{\rm de}|_{1000\ \rm Torr} < \tilde{P}_{x,\rm av}^{\rm de}|_{2000\ \rm Torr}$). However, the dependence of $\tilde{P}_{x,\rm av}^{\rm de}$ on the N_2 pressure is not monotonic, because $P_x^{\rm de} = \gamma_e B P_e^{\rm de}/(R_{\rm op} + \Gamma_{\rm rel})$ when ignoring the spatial dependence and $\Gamma_{\rm rel}$ is larger with more buffer gas. Therefore, $\tilde{P}_{x,\rm av}^{\rm de}|_{3000\ \rm Torr} < \tilde{P}_{x,\rm av}^{\rm de}|_{2000\ \rm Torr}$ since the increase in $\Gamma_{\rm rel}$ has a greater influence than the suppression of the wall-depolarization effect.

The optimal transverse signal $\tilde{P}_{x,\rm av}^{\rm de}$ for depolarizing walls can be estimated analytically as (see Appendix B for details)

$$\tilde{P}_{x,\rm av}^{\rm de} \approx \min\{r_1, r_2\}, \tag{16}$$

where

$$r_1 = \max\left(\frac{P_{\rm av}^{\rm de}}{P_{\rm av}^{\rm nonde}}\frac{\gamma_e B R_{\rm op}^0}{\left(R_{\rm op}^0 + \Gamma_{\rm rel}\right)^2}\right)$$

and

$$r_2 = \max\left(\frac{P_{\rm av}^{\rm de}}{P_{\rm av}^{\rm nonde}}\frac{\gamma_e B}{2\left(R_{\rm op}^0 + \Gamma_{\rm rel}\right)}\right). \tag{17}$$

This analytical upper bound of $\tilde{P}_{x,\rm av}^{\rm de}$ is shown in Fig. 7(a), which has up to 30% deviation from the exact numerical values. Therefore, using the simple expression (16) can be helpful to determine the optimal parameters without solving the nonlinear equations. It should be noted that even with optimized parameters, the transverse signal for depolarizing walls can be significantly smaller than the nondepolarizing-wall case. For example, for 100 Torr and 200 Torr N_2, which are sufficient to suppress radiation trapping, the latter case is presented in Fig. 7(b). In this case, the signal $P_{x,\rm av}^{\rm nonde}$ can be one order of magnitude larger than $\tilde{P}_{x,\rm av}^{\rm de}$ due to the strong wall-depolarizing effect in small vapor cells.

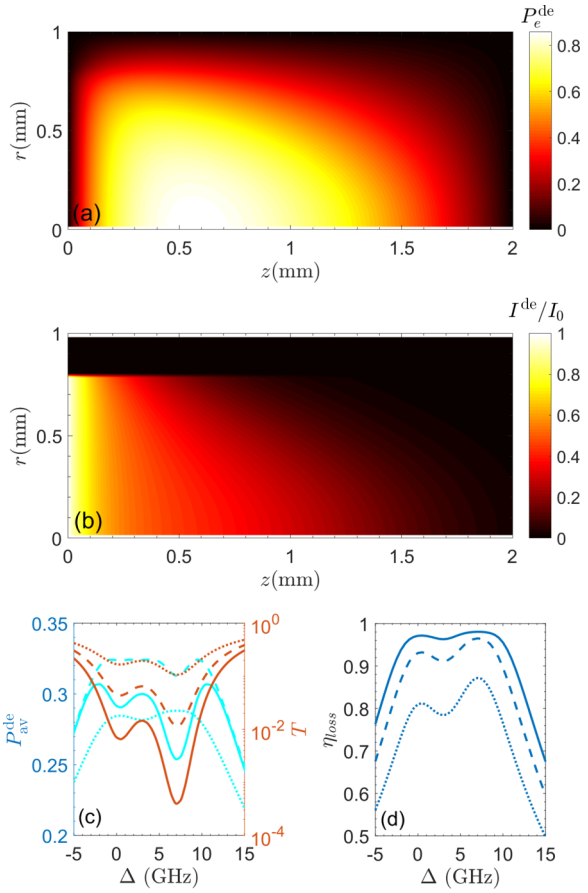

FIG. 8. (a) Spatially dependent atomic polarization $P_e^{\rm de}(z, r)$ of ^{87}Rb and (b) normalized light intensity $I^{\rm de}(z, r)/I_0$ for partially illuminated, uncoated cells with laser beam radius $r_L = 0.8$ mm and the other parameters the same as in Fig. 2(a). (c) Average polarization $P_{\rm av}^{\rm de}$ (light blue lines) and the transmission probability T (dark red line). (d) Light loss $\eta_{\rm loss}$ by the depolarizing wall. Here the radii r_L are 0.8 mm (solid lines), 0.6 mm (dashed lines), and 0.4 mm (dotted lines).

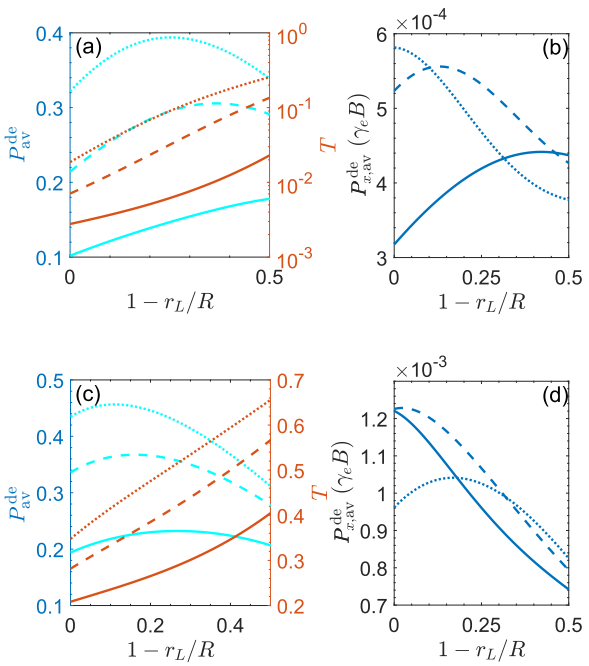

FIG. 9. Average atomic polarization $P_{\rm av}^{\rm de}$ of ^{87}Rb (light blue lines), pump laser's transmission probability T (dark red lines), and transverse signal $P_{x,\rm av}^{\rm de}$ of SERF magnetometers at different N_2 pressures and input powers. The N_2 pressures are (a) and (b) 500 Torr and (c) and (d) 2000 Torr. The laser input powers are 0.1 mW (solid line), 0.2 mW (dashes line), and 0.3 mW (dotted line).

IV. PARTIALLY ILLUMINATED CELLS

Uncoated cells exhibit depolarization of atoms in the vicinity of the boundary, within a distance of λ_D. To mitigate this wall-depolarizing effect, the laser beam can be concentrated on the central region of the cell while maintaining constant input power or I_{in}. To demonstrate this, we simulate the atomic polarization $P_e^{\rm de}(z, r)$ and the light intensity $I^{\rm de}(z, r)/I_0$, with a laser radius of 0.8 mm and input power of 0.5 mW, depicted in Figs. 8(a) and 8(b), respectively. While the light is confined to the central region of the cell due to radial nonpropagation, the atomic polarization in the unilluminated region is still nonzero as spins diffuse in all directions via collisions. Note that the incident light intensity I_0 is dependent on the illumination area as $I_0 = I_{\rm in}/\pi r_L^2$. Our results show that the partially illuminated cell exhibits more centralized atomic polarization and a slower rate of decay of the light intensity $I^{\rm de}(z, r)/I_0$ in the z direction, as compared to Figs. 2(a) and 2(b). The overall effect is depicted in Figs. 8(c) and 8(d), where the average polarization $P_{\rm av}^{\rm de}$ and light transmission T are both increased, resulting in a reduced light loss $\eta_{\rm loss}$ due to the wall.

The impact of centralizing the laser beam on the wall-depolarizing effect is most evident at resonant points that correspond to absorption peaks. This is highly beneficial for compact atomic-vapor-cell-based devices, the frequency of which is locked to absorption peaks. In this study we examined the polarization $P_{\rm av}^{\rm de}$ at the absorption peaks and the transverse signal $P_{x,\rm av}^{\rm de}$ of the SERF magnetometer under various input powers and N_2 pressures.

As r_L decreases, the effective absorption length increases and the wall-polarization effect is reduced, leading to a higher polarization $P_{\rm av}^{\rm de}$. However, once the polarization centralized around the illuminating region approaches its maximum value, the total polarization begins to decrease. Meanwhile, reducing the light lost due to wall depolarizing by monotonically decreasing r_L results in a significant increase in the transmission probability. This increase is particularly noticeable at low N_2 densities [500 Torr in Figs. 9(a) and 9(b)]. For example, with 0.2 mW of input power (dashed lines), $P_{\rm av}^{\rm de}$ increases from 0.21 to 0.31 when the beam radius is reduced from R to $0.65R$, while T increases from 0.007 to 0.06. This one-order increase in transmission probability is advantageous in locking the laser's frequency. Furthermore, reducing r_L also results in an increase in the signal $P_{x,\rm av}^{\rm de}$. These characteristics of $P_{\rm av}^{\rm de}$, T, and $P_{x,\rm av}^{\rm de}$ are consistent across different N_2 densities [2000 Torr in Figs. 9(c) and 9(d)], although their changes with respect to r_L are less significant since the wall-depolarizing effect is smaller when more buffer gas is present.

V. CONCLUSION

In this work we have investigated the wall effect in small atomic vapor cells at high temperatures. By comparing cases with fully depolarizing and nondepolarizing walls, we found that the traditional treatment, which considers only the lowest diffusion mode, underestimates the wall-depolarizing effect in the 2-mm cells. To address this issue, we proposed a theoretical estimation of the ratio between the polarizations for depolarizing and nondepolarizing boundaries.

To demonstrate practical implications of our findings, we focused on the SERF magnetometer and its transverse signal dependence on the wall effect. We derived a theoretical upper bound for the uncoated cells, which revealed that the optimal signal for cells with depolarizing walls is one order smaller compared to that of nondepolarizing walls. Our study also presented an approach to reduce the wall-depolarizing effect by shrinking the beam's radius while maintaining its input power, in addition to detuning the pump laser. This method can enhance various physical quantities concerned, such as the atomic polarization, the transmission probability, and the transverse signal of the SERF magnetometer.

ACKNOWLEDGMENTS

This work was supported by the National Natural Science Foundation of China under Grants No. U2141237 and No. 62101070.

APPENDIX A: ABSORPTION AND POLARIZATION PEAKS FOR NONDEPOLARIZING WALLS

In this Appendix we prove that the absorption and polarization peaks for nondepolarizing walls are at $\partial_\Delta \mathcal{L}(\Delta) = 0$. We first integrate Eq. (2) and acquire

$$I(L) = I(0)\exp\left(-g_I \mathcal{L}(\Delta)\int_0^L dz[1 - P_e(z)]\right). \tag{A1}$$

Note that for nondepolarizing cylindrical boundaries, I and P_e are uniformly distributed in the radial direction, so they are only functions of z. Then the derivative of Eq. (A1) $\partial_\Delta I(L)$ reads

$$\partial_\Delta I(L) = g_I I(L)[\mathcal{L}(\Delta)\partial_\Delta \int_0^L dz\, P_e(z) - \int_0^L dz[1 - P_e(z)]\partial_\Delta \mathcal{L}(\Delta)]. \tag{A2}$$

At the peaks, $\partial_\Delta I(L) = 0$ and equivalently $\partial_\Delta \int_0^L dz\, P_e(z) = 0$ [see Eq. (9) for the uniform irradiation case], which consequently gives

$$\int_0^L dz[1 - P_e(z)]\partial_\Delta \mathcal{L}(\Delta) = 0. \tag{A3}$$

Since $1 - P_e(z) > 0$, the maximal polarization or absorption is at $\partial_\Delta \mathcal{L}(\Delta) = 0$.

APPENDIX B: ESTIMATION OF $P_{\rm av}^{\rm de}/P_{\rm av}^{\rm nonde}$ AND $\tilde{P}_{x,\rm av}^{\rm de}$

To acquire an analytical estimation of the ratio $P_{\rm av}^{\rm de}/P_{\rm av}^{\rm nonde}$, we first simplify Eq. (1) by assuming the light intensity is unchanged in the vapor cell and neglecting the derivative of the slow-down factor $q(P_e)$. Under these approximations, we can express $P_e^{\rm de}$ for depolarizing boundaries as $P_e^{\rm de} = f_{xy}(x, y)f_z(z)$, where its longitudinal dependence is given by

$$f_z(z) = \frac{\tilde{R}_{\rm op}}{\tilde{R}_{\rm op} + \Gamma_{\rm rel}}\left(1 - \frac{e^{-z/\lambda_D} + e^{-(L-z)/\lambda_D}}{1 + e^{-L/\lambda_D}}\right), \tag{B1}$$

with $\tilde{R}_{\rm op} \equiv g_P \mathcal{L}(\Delta) I_0$. This simplified solution shows that the depolarizing wall only affects a layer with a width of λ_D. Though the solution for the radial direction is more complicated, we can assume that the influence of the depolarizing wall is similar. Hence, the unaffected. volume can be estimated as

$$\pi(R - \lambda_D)^2(L - 2\lambda_D). \tag{B2}$$

Up until now, we have assumed an overall constant light intensity I_0 in the cell. However, the wall-depolarization length λ_D should be larger because I decays in both the radial and longitudinal directions. This decay is faster when the light is closer to the walls where the polarization is small, and we can characterize it using the absorption length λ_L. Accounting

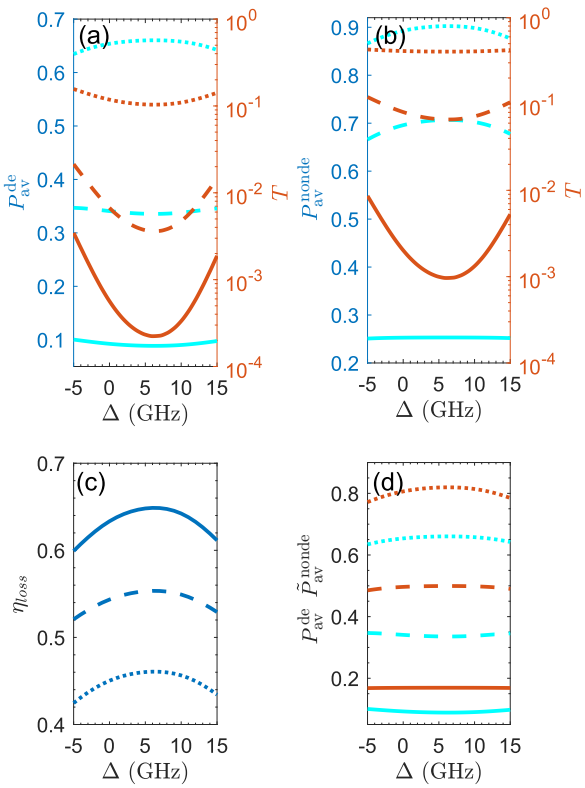

FIG. 10. Average polarization $P_{\rm av}^{\rm de}$ of ^{133}Cs [light blue lines in (a)], transmission probability T [dark red lines in (a)], and fraction $\eta_{\rm loss}$ of pump laser absorbed by the cell walls [in (b)] for depolarizing walls. (c) As a contrast, $P_{\rm av}^{\rm nonde}$ and T for nondepolarizing walls are shown. (d) Average polarization $\tilde{P}_{\rm av}^{\rm nonde}$ (dark red lines) for nondepolarizing walls by including $\Gamma_{\rm wall}$ (with slow-down factor $q = 22$) in the longitudinal decay. In comparison, $P_{\rm av}^{\rm de}$ is also shown (light blue lines). Here the cell's temperature is 150 °C, the N_2 pressure is 1000 Torr, and the laser input powers are 0.5 mW (solid line), 1.5 mW (dashes line), and 03 mW (dotted line).

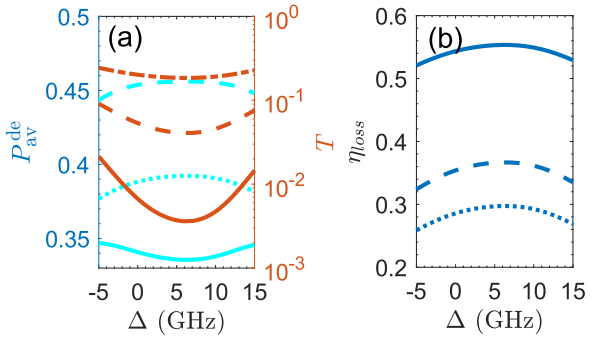

FIG. 11. Average polarization P_{av}^{de} of ^{133}Cs [light blue lines in (a)], transmission probability T [dark red line in (a)], and light loss η_{loss} absorbed by the depolarizing wall [in (b)] for partially illuminated cells. Here the N_2 pressure is 1000 Torr and the laser input power is 1.5 mW, with radii r_L equal to 0.8 mm (dashed lines) and 0.6 mm (dotted lines). In comparison, P_{av}^{de} and T for fully illuminated cells are shown with solid lines.

for this by including a factor of $\sqrt{1-\lambda_D/\lambda_L}$ in the ratio $P_{av}^{de}/P_{av}^{nonde}$, we obtain

$$\frac{P_{av}^{de}}{P_{av}^{nonde}} \approx \sqrt{1-\frac{\lambda_D}{\lambda_L}}\frac{\pi(R-\lambda_D)^2(L-2\lambda_D)}{\pi R^2 L} = \sqrt{1-\frac{\lambda_D}{\lambda_L}}\left(1-2\frac{\lambda_D}{L}\right)\left(1-\frac{\lambda_D}{R}\right)^2. \quad \text{(B3)}$$

For SERF magnetometers, if we ignore the spatial dependence of the light intensity and the atomic polarization, the optimal transverse signal

$$\tilde{P}_x = \frac{\gamma_e B}{2(R_{op}+\Gamma_{rel})},$$

while the z-direction polarization is 1/2. Taking into account the wall-depolarizing effect, a factor $P_{av}^{de}/P_{av}^{nonde}$ is added and the largest transverse signal $\tilde{P}_{x,av}^{de}$ for depolarizing walls becomes

$$\tilde{P}_{x,av}^{de} \approx \max\left(\frac{P_{av}^{de}}{P_{av}^{nonde}}\frac{\gamma_e B}{2(R_{op}^0+\Gamma_{rel})}\right). \quad \text{(B4)}$$

However, for high densities of N_2, Eq. (B4) may overestimate the maximal $P_{x,av}^{de}$. Returning to the full expression for the spatial-independent transverse signal

$$P_x = \frac{\gamma_e B R_{op}}{(R_{op}+\Gamma_{rel})^2}, \quad \text{(B5)}$$

we obtain Eq. (16).

APPENDIX C: WALL EFFECT FOR CESIUM

To illustrate the wall effect on uncoated vapor cells with other alkali-metal atoms, we plot the polarization of ^{133}Cs in a cell also heated to 150 °C. The cell size is the same as the rubidium cell and the pressure of the nitrogen gas is 1000 Torr. Since the density of cesium is higher (about twice the density of rubidium) compared to ^{87}Rb, the polarization of ^{133}Cs is smaller due to its larger optical depth, along with less light transmission and more loss of the pump laser on the depolarizing wall. As a comparison, the polarization for nondepolarizing walls and the transmission probability of the pump laser are shown in Fig. 10(c). Note that even by including a wall-relaxation rate Γ_{wall} in the longitudinal decay rate Γ_{rel} (the slow-down factor is taken to be 22, the largest for ^{133}Cs) for the nondepolarizing-wall cells, the average polarization $\tilde{P}_{av}^{nonde}$ is much larger than the depolarizing-wall case. Therefore, the wall effect is underestimated by considering only Γ_{wall}.

Similar to rubidium, the wall effect for cesium cells can be mitigated by reducing the pump beam's radius while maintaining its input power. This is demonstrated in Fig. 11.

[1] I. K. Kominis, T. W. Kornack, J. C. Allred, and M. V. Romalis, Nature (London) **422**, 596 (2003).
[2] D. Budker, Nature (London) **422**, 574 (2003).
[3] D. Budker and M. Romalis, Nat. Phys. **3**, 227 (2007).
[4] W. Happer, E. Miron, S. Schaefer, D. Schreiber, W. A. van Wijngaarden, and X. Zeng, Phys. Rev. A **29**, 3092 (1984).
[5] T. G. Walker and W. Happer, Rev. Mod. Phys. **69**, 629 (1997).
[6] S. Appelt, A. B.-A. Baranga, C. J. Erickson, M. V. Romalis, A. R. Young, and W. Happer, Phys. Rev. A **58**, 1412 (1998).
[7] V. V. Yashchuk, J. Granwehr, D. F. Kimball, S. M. Rochester, A. H. Trabesinger, J. T. Urban, D. Budker, and A. Pines, Phys. Rev. Lett. **93**, 160801 (2004).
[8] J. Vanier and C. Tomescu, *The Quantum Physics of Atomic Frequency Standards: Recent Developments* (CRC, Boca Raton, 2015).
[9] P. Forman, Science **249**, 685 (1990).
[10] B. Julsgaard, J. Sherson, J. I. Cirac, J. Fiurášek, and E. S. Polzik, Nature (London) **432**, 482 (2004).
[11] K. Hammerer, A. S. Sørensen, and E. S. Polzik, Rev. Mod. Phys. **82**, 1041 (2010).
[12] C. B. Møller, R. A. Thomas, G. Vasilakis, E. Zeuthen, Y. Tsaturyan, M. Balabas, K. Jensen, A. Schliesser, K. Hammerer, and E. S. Polzik, Nature (London) **547**, 191 (2017).
[13] N. Fortson, P. Sandars, and S. Barr, Phys. Today **56**(6), 33 (2003).
[14] J. M. Amini, C. T. Munger, and H. Gould, Phys. Rev. A **75**, 063416 (2007).
[15] B. M. Roberts, V. A. Dzuba, and V. V. Flambaum, Annu. Rev. Nucl. Part. Sci. **65**, 63 (2015).
[16] W. Happer, Y.-Y. Jau, and T. Walker, *Optically Pumped Atoms* (Wiley, New York, 2010).
[17] M. Auzinsh, D. Budker, and S. M. Rochester, *Optically Polarized Atoms: Understanding Light-Atom Interactions* (Oxford University Press, New York, 2010).
[18] Z. Wu, Rev. Mod. Phys. **93**, 035006 (2021).
[19] J. Keaveney, I. G. Hughes, A. Sargsyan, D. Sarkisyan, and C. S. Adams, Phys. Rev. Lett. **109**, 233001 (2012).
[20] T. Peyrot, Y. R. P. Sortais, J.-J. Greffet, A. Browaeys, A. Sargsyan, J. Keaveney, I. G. Hughes, and C. S. Adams, Phys. Rev. Lett. **122**, 113401 (2019).

[21] E. Klinger, H. Azizbekyan, A. Sargsyan, C. Leroy, D. Sarkisyan, and A. Papoyan, Appl. Opt. **59**, 2231 (2020).
[22] M. Auzinsh, A. Sargsyan, A. Tonoyan, C. Leroy, R. Momier, D. Sarkisyan, and A. Papoyan, Appl. Opt. **61**, 5749 (2022).
[23] S. J. Seltzer, *Developments in Alkali-Metal Atomic Magnetometry* (Princeton University Press, Princeton, 2008).
[24] S. Seltzer and M. Romalis, J. Appl. Phys. **106**, 114905 (2009).
[25] M. E. Wagshul and T. E. Chupp, Phys. Rev. A **49**, 3854 (1994).
[26] R. Knize, Z. Wu, and W. Happer, in *Advances in Atomic and Molecular Physics*, edited by D. Bates and B. Bederson (Elsevier, Amsterdam, 1988), Vol. 24, pp. 223–267.
[27] W. Franzen, Phys. Rev. **115**, 850 (1959).
[28] W. Happer and A. C. Tam, Phys. Rev. A **16**, 1877 (1977).
[29] J. C. Allred, R. N. Lyman, T. W. Kornack, and M. V. Romalis, Phys. Rev. Lett. **89**, 130801 (2002).
[30] I. M. Savukov and M. V. Romalis, Phys. Rev. A **71**, 023405 (2005).
[31] Y. Chang, Y.-H. Guo, and J. Qin, Phys. Rev. A **99**, 063411 (2019).
[32] A. F. Molisch and B. P. Oehry, *Radiation Trapping in Atomic Vapours* (Oxford University Press, Oxford, 1998).
[33] W. Lee, *Ultra-high Sensitivity Atomic Magnetometers* (Princeton University Press, Princeton, 2022).